

1                   Is the Aftershock Zone Area a Good Proxy for the  
2                                   Mainshock Rupture Area?

3                   Jing Ci Neo<sup>1</sup>, Yihe Huang<sup>1</sup>, Dongdong Yao<sup>1</sup>, Shengji Wei<sup>2</sup>

4                   [1] University of Michigan, Ann Arbor. 1100 North University, Room 4534F

5                   [2] Asian School of the Environment, Nanyang Technological University. Earth Observatory of Singapore, 50

6                                   Nanyang Avenue, Block N2-01a-15

7  
8                   This paper is a non-peer reviewed preprint submitted to EarthArXiv. It has been submitted to Bulletin of  
9                   Seismological Society America (BSSA) and is currently undergoing peer review.

10

11 **Abstract** Large earthquakes are usually followed by sequences of small earthquakes, exhibiting  
12 a mainshock-aftershock pattern. The locations of aftershocks are often observed to be on the same  
13 fault plane as the mainshock and used as proxies for its rupture area. However, there has been  
14 limited research on how well aftershock location actually approximates mainshock rupture area.  
15 Furthermore, recent developments in earthquake relocation techniques have led to great  
16 improvements in the accuracy of earthquake locations. Hence, we investigate this assumption  
17 using slip distributions and relocated aftershocks of 12  $M_w \geq 5.4$  mainshocks in California. We  
18 calculate the area enclosed by the aftershocks, normalized by the mainshock rupture area derived  
19 from slip contours. We find that overall, the ratios of aftershock zone area to mainshock rupture  
20 area, hereinafter referred to as “aftershock ratio”, lie within a range of 0.5 to 5.5, with most values  
21 larger than 1. Using different slip inversion models for the same earthquake can have a large impact  
22 on the results, but the ratios estimated from both the relocated catalogs and Advanced National  
23 Seismic System (ANSS) catalog have similar patterns. The ratios for earthquakes in Southern  
24 California fall between 0.5 and 3, while earthquakes in Northern California exhibit a wider range  
25 of ratios from 1 to 5.5. We also measure aftershock ratios for the early aftershock window (within  
26 1 day) and find a similar range but smaller values than using the entire aftershock duration,  
27 suggesting that continuing afterslip could contribute to the expanding aftershock zone area of  
28 several mainshocks. Our results show that areas with positive Coulomb stress change scale with  
29 aftershock zone areas, indicating that aftershock distribution generally outlines the mainshock  
30 rupture area.

## 31 **1. Introduction**

32 Beginning in the 1930s, scientists believed that aftershock zone area corresponds to the area where  
33 strain is accumulated and released during an earthquake sequence (Utsu, 1970). Since then, the  
34 aftershock zone area of a mainshock has often been used to approximate its co-seismic rupture  
35 area. For example, Kanamori (1977) used the rupture zones defined by the 1-day aftershock zone

36 area to calculate seismic moment and introduce the moment magnitude scale. Kelleher (1972)  
37 attempted to forecast potential locations of large South American earthquakes by discerning gaps  
38 between their rupture zones, which were defined by the aftershock zone area. Ebel and Chambers  
39 (2016) suggested that aftershocks of past major earthquakes can be used to delineate the extent of  
40 their ruptures even after decades or centuries. Studies have also found that early aftershocks  
41 (within the first 24 hours) tend to occur on the periphery of the aftershock zone, and the aseismic  
42 region in the center of the zone corresponds to the extent of the coseismic rupture area (Das and  
43 Henry, 2003; Dietz and Ellsworth, 1990).

44 Different mechanisms have been used to explain various patterns of aftershock occurrence: static  
45 stress change, transient dynamic stress change, and postseismic deformation are possible  
46 candidates (Freed, 2005). Static stress change is the stress change in the earth's crust surrounding  
47 the fault planes due to slip on the faults (King et al., 1994; etc.). In particular, Coulomb stress  
48 change became popular in the past few decades with numerous studies attempting to correlate  
49 static Coulomb stress change with aftershocks (King et al., 1994; Stein et al., 1997; Hardebeck et  
50 al., 1998; Toda et al., 1998; Kilb et al., 2002; Ma et al., 2005; Marsan and Lengliné, 2010; Toda  
51 et al., 2011, etc.). Many of the studies found that the distribution of the aftershocks appears to be  
52 co-located with regions of positive Coulomb stress change.

53 However, not all studies agree that static stress change is the only predictor of aftershock  
54 distribution, especially the temporal evolution of aftershocks (Cattania et al., 2015). Transient  
55 dynamic stress change, which is the stress carried by the passing waves, can trigger "aftershocks"  
56 hundreds to thousands of kilometers away and may be related to earthquakes at those locations  
57 even months later (Berlardinelli et al, 2003; Parsons, 2014; Fan and Shearer, 2016; van der Elst  
58 and Brodsky, 2010). Moreover, by investigating over two hundred slip inversions, Meade et al.  
59 (2017) found that other stress change components such as max shear stress and stress invariants,

60 or longer-term changes such as afterslip/postseismic relaxation may be able to account for the  
61 spatial distribution of aftershocks better.

62 Afterslip is the continuing fault slip after the mainshock, and viscoelastic relaxation refers to the  
63 release of stress throughout the entire volume of the surrounding viscous lower crust under  
64 constant strain (Pollitz et al., 1998; Diao et al., 2013). Both processes have been shown to be able  
65 to explain aftershocks distributions. The contribution of each of them is hard to determine, and it  
66 depends on the tectonic regime of each earthquake (Perfettini et al 2005). For example, Perfettini  
67 and Avouac (2004; 2007) found that the aftershocks of the 1999 Chi-Chi earthquake and the 1992  
68 Landers earthquake correlate well with afterslip in both space and time. Savage et. al. (2007)  
69 investigated five large earthquakes and concluded that fault creep alone is not enough to explain  
70 the postseismic deformation and aftershocks of those earthquakes; a viscoelastic relaxation term  
71 has to be added to the surface deformation equation to obtain a better fit.

72 However, quantitative models of afterslip and viscoelastic relaxation are less observed and  
73 resolved. In this study, we will quantify static Coulomb stress change from mainshock slip and  
74 evaluate whether the aftershock zone area could be used as a proxy of the mainshock rupture.  
75 Meanwhile, we summarize those published work on afterslip models for some mainshocks and  
76 discuss their roles in modulating the aftershock distribution.

77 The selection of aftershock duration and method to delineate aftershock zone are main factors that  
78 affect the calculation of the aftershock zone area. Scientists have previously pointed out that there  
79 was no formal agreement on a consistent space-time windowing algorithm to select aftershocks  
80 (Knopoff et al., 1982), which is still true to this date. The choice of aftershock duration is tricky  
81 as the aftershock zone area could expand with time (Tajima and Kanamori, 1985), and different  
82 mechanisms could tangle together with longer durations. Different aftershock durations ranging  
83 from one day (Kanamori, 1977), weeks (Wetzler et al, 2018) to years (Parsons, 2002; Perfettini

84 and Avouac, 2007) have been used, depending on the need of each study. Some studies suggested  
85 that earthquakes may still have aftershocks decades or centuries later (Bouchon et al., 2013; Ebel  
86 and Chambers, 2016). Determining aftershock zone area is difficult too as aftershocks can occur  
87 over a large and continuous area especially in places with high background seismicity such as  
88 Parkfield, and deciding which earthquakes constitute aftershocks can be quite challenging.  
89 Methods used by previous studies include fitting ellipses (Utsu, 1970), drawing energy contours  
90 (Tajima and Kanamori, 1985), terminating the aftershock zone based on gaps between the  
91 earthquakes (Meng and Peng, 2016), or drawing a simple boundary around the aftershocks (Sykes,  
92 1971). In this study, we use the beta statistic (Matthews and Reasenber, 1998) to estimate the  
93 aftershock duration and aftershock boundary based on the change in seismicity rate after the  
94 mainshock since it provides a consistent criterion without empirical assumption.

95 More recently, developments in seismological techniques have also led to great improvements in  
96 the accuracy of earthquake locations and finite fault solutions. This provides an opportunity to  
97 reexamine past assumptions using the latest earthquake catalogs and slip models. In this study, we  
98 analyze recent moderate to large ( $M_w \geq 5.4$ ) earthquakes in California that have relocated  
99 earthquake catalogs (Figure 1). We aim to gain insights into earthquake properties and assess the  
100 veracity of the assumptions made in the past. Our results can also provide basis for similar  
101 assumptions to be made in the future, especially in cases where robust slip inversion is not  
102 applicable.

## 103 **2. Data and Method**

104 We analyze moderate to large ( $M_w \geq 5.4$ ) earthquakes in California that have well recorded  
105 aftershock sequences as candidate mainshocks (Figure 1). The slip inversion models are obtained  
106 from the Finite-Source Rupture Model Database (SRCMOD). On the other hand, we use both  
107 relocated catalog (either double-difference or waveform relocated) and Advanced National

108 Seismic System (ANSS) catalog for following analysis. The relocated catalogs generally have  
109 better resolved locations. However, a certain percentage of earthquakes would be dropped during  
110 the relocation process and potentially affect the genuine seismicity rate estimation. The ANSS  
111 catalog includes all archived earthquakes but endures relatively larger location error. We included  
112 both catalogs to evaluate the consistency. More specifically, the double-difference catalogs are  
113 acquired from the Northern California Earthquake Data Center (NCEDC) (Waldhauser and Schaff,  
114 2008; Waldhauser, 2009). Waveform relocated catalogs are obtained from the Southern California  
115 Earthquake Data Center (SCEDC) (Hauksson et al., 2012). For each mainshock, we download  
116 earthquakes that occurred up to 1 year before and after within the surrounding area. The areas used  
117 is deliberately much larger than needed to avoid creating an artificial upper limit when calculating  
118 the aftershock zone area. A grid of  $\pm 1$ -degree latitude and longitude relative to the mainshock  
119 epicenter is used to download earthquakes from NCEDC/SCEDC, while a circle with a radius of  
120 five times the source dimension is used to download earthquakes from the ANSS catalog.

### 121 *Earthquake Selection*

122 To choose earthquakes associated with mainshock faults, only earthquakes with off-fault distances  
123 less than 2km to the fault plane from the slip inversion are kept for further analysis. We use 2km  
124 because earthquake epicenter location uncertainties typically fall within 2km. We have tried  
125 different off-fault distances from 1 to 20km and found that off-fault distances below 5km do not  
126 show a large difference. As hypocenter locations given by the slip inversion data and the catalogs  
127 are slightly different, we shift the earthquake locations in the catalog using the hypocenter in the  
128 slip inversion as a reference for some mainshocks. This ensures that the selection of earthquakes  
129 by off-fault distance is accurate and does not affect the calculation of the aftershock zone area. The  
130 fault planes are extrapolated past each end, and the earthquakes are then projected onto the nearest  
131 fault plane (i.e., smallest fault-normal distance).

### 132 ***Magnitude of Completeness***

133 To remove bias in calculating the change in seismicity rate, we need to ensure that the catalog is  
134 complete for both the periods before and after the mainshock, i.e. there are no missing earthquakes  
135 for the magnitude range we use. Hence, we calculate the magnitude of completeness ( $M_c$ ) for both  
136 time periods, and only earthquakes with magnitudes above the larger  $M_c$  are used. In a few cases,  
137  $M_c$  cannot be calculated for either before or after the mainshock, due to the sparsity of data or the  
138 shape of the magnitude-frequency distribution (MFD). Hence, we use  $M_c$  of the time period that  
139 can be calculated instead. The most straightforward way of calculating  $M_c$  is the maximum  
140 curvature method, which often underestimates  $M_c$  for gradually curved bulk MFDs. The  $M_{c95}$   
141 and  $M_{c90}$  methods, which calculate the lowest  $M_c$  value that gives a best fit of 95% and 90%,  
142 provide a closer estimate, but sometimes  $M_c$  cannot be calculated when the MFD curve never  
143 reaches a 90% fit. Hence, we use the best combination method, whereby an initial estimate is  
144 calculated using the max curve, and then the algorithm searches for the  $M_{c95}$  value and  $M_{c90}$   
145 value in a fixed range around the estimate. These methods are described in detail in Mignan and  
146 Woessner (2012), and we use the open-source MATLAB code written by D. Schorlemmer and J.  
147 Woessner (2004) to calculate  $M_c$ . We set the magnitude bin size to be 0.1 and do not apply any  
148 correction.

### 149 ***Beta Statistic and Aftershock Ratio***

150 We use the  $\beta$ -Statistic to calculate the aftershock zone area. The  $\beta$ -statistic quantifies seismicity  
151 rate change based on the difference between the observed and expected number of events occurring  
152 in a time period, normalized by the standard deviation of the expected value (Aron and Hardebeck,  
153 2009; Kilb et al., 2000). The standard deviation is calculated by assuming a binomial distribution  
154 where earthquakes either occur inside or outside the time period  $T_a$  (Matthews and Reasenber,  
155 1988). A  $\beta$  value of 2, which means 95% significance of increase in seismicity when the  $\beta$  value

156 is normalized by its standard deviation, is used as the threshold to determine if there is a significant  
157 increase in seismicity. The equation to calculate the  $\beta$  value is shown below (Equation 1).

$$158 \quad \beta = \frac{N_a - N * T_a / T}{\sqrt{N(T_a / T)(1 - T_a / T)}} \quad (1)$$

159 Where  $N_a$  is the number of events in the time period of interest,  $N$  is the number of events in the  
160 entire time period,  $T_a$  is the duration of the time period of interest and  $T$  is the duration of the  
161 entire time period (background window duration  $T_b$  plus above defined  $T_a$ ).  
162

163 We define the aftershock zone as the region with significant increase in seismicity rate after the  
164 mainshock. To find the aftershock zone, we create a grid for the fault plane and the surrounding  
165 regions and calculate the  $\beta$  value for each grid cell. A convex boundary is then drawn around those  
166 areas with significant change in seismicity using the MATLAB function “boundary” with a ‘shrink  
167 factor’ of 0, which is consistent with results using Delaunay triangulation to denote the boundary.  
168 The area enclosed by the boundary is then taken to be the aftershock zone area. Another possible  
169 method of calculating the aftershock area is to add up area of cells with significant seismicity rate  
170 increase. However, we chose not to use this method mainly because the aftershock zone area  
171 increases with cell size, which could be subjective to provide a consistent way to estimate  
172 aftershock zone area spanning different magnitudes (Figure S1). In comparison, drawing a  
173 boundary around the aftershocks is a robust way to define the aftershock zone area that is largely  
174 unaffected by cell size (Table S1). Figure 2 illustrates the calculation of the aftershock zone area.  
175 Previous calculations of  $\beta$  values have used different cell sizes such as 2 km (Aron and Hardebeck,  
176 2009) and 6 km (Kilb et al., 2000). As earthquakes are represented as points in the grid, the choice  
177 of cell size has an impact on the  $\beta$  values. Using different cell sizes that range from 1 to 4 km, we  
178 find that as long as the cell size is large enough such that each earthquake is not isolated, the pattern  
179 of  $\beta$  values remains similar. However, a larger cell size like 6 by 6 km (Kilb et al., 2000) is not  
180 ideal as it is close to the rupture length of the mainshock, which ranges from 9 to over 100 km in



181 our analysis. Hence, we use a cell size of 2 by 2 km. We locate the areas where the  $\beta$  value is  
182 larger than 2 and terminate the aftershock zone area when there is a gap of larger than 15 km  
183 (Meng and Peng, 2016). We test a range of gap sizes from 5 to 20 km and find that for small off-  
184 fault distances ( $\leq 5$  km), and the gap size does not affect the results.

185 The choice of time periods  $T$  and  $T_a$  can greatly affect the calculation of the aftershock zone area  
186 by controlling the number of earthquakes that constitute change in seismicity rate. To estimate the  
187 background seismicity rate, we adopt a long-term averaged rate before the mainshock. Previous  
188 studies reported obvious increasing foreshocks before some large earthquakes (e.g., Dodge et al.,  
189 1995; Hauksson et al., 2002, etc.). However, the short-term foreshock activity should not  
190 significantly impact our calculation since we use a much longer window before the mainshock. To  
191 test this, we use background window lengths of one year and two years and found that the ratios  
192 are generally consistent except for the Whittier Narrows and North Palm Springs earthquake  
193 (Figure S2). The range of ratios also remain the same using both pre-shock windows. Since using  
194 a pre-shock duration of one year generates more consistent results between the relocated and non-  
195 relocated catalogs, we use a pre-shock duration of one year to calculate  $\beta$  values and aftershock  
196 zone areas.

197 Another important parameter is the aftershock duration, which defines the time period when there  
198 is still a significantly elevated rate of seismicity in the region. We then calculate the sliding-  
199 window  $\beta$  value for the entire faulting system (fault plane and the extended regions) using the  
200 aftershocks within an off-fault distance of 2km, with  $N$  in equation (1) equal to all the earthquakes  
201 that occurred in the region and  $T_a$  equal to 10 days after the mainshock. We then slide the time  
202 window with a time interval of 5 days and study the evolution of the  $\beta$  value through time. The  
203 defined entire aftershock duration is given by the first time-window when the  $\beta$  value drops below  
204 the threshold value of 2. The aftershock duration gives  $T_a$ , the time period of interest used in the

205 calculation of the  $\beta$  value in each grid cell for each earthquake. The aftershock duration can vary  
206 between a few weeks and over a year (Figure 3).

207 The coseismic rupture area is defined as the area enclosed by a contour of 0.15 of the maximum  
208 slip (Wetzler et al., 2018). A slip contour is used because areas with very low slip may not be well  
209 resolved and depend greatly on the smoothing method used in the kinematic source inversion. We  
210 then calculate the ratio of the aftershock zone area to the coseismic rupture area to investigate how  
211 well the aftershock zone area approximates the rupture area. Since each earthquake model is  
212 unique, some of them require special processing procedures as listed in Table S2.

### 213 *Coulomb Stress Change*

214 In order to examine how the mainshock slip impacts the aftershock zone area, we utilize the  
215 Coulomb 3 software to calculate the resulting Coulomb stress change of each earthquake (King et  
216 al, 1994). We use the entire slip model and the orientation of the main fault plane as the receiver  
217 fault to find the Coulomb stress change of the region. Assuming that earthquakes below a certain  
218 off-fault distance lie on the same fault plane as the mainshock, we use the orientation of the main  
219 fault plane as the receiver fault to find the Coulomb stress change of the region. We also use a  
220 friction coefficient of 0.6, although faults have a large range of plausible values between 0 to 0.75  
221 (King et al, 1994). The cross-section of the fault and its surrounding region are calculated with a  
222 cell size of 1 by 1 km. We tested thresholds of 0.1 and 1 MPa and find that both will result in a  
223 similar trend, but the area enclosed by the 1 MPa cells are more similar to the aftershock zone area  
224 observed from the  $\beta$ -Statistic. Hence, we sum the area of the cells that have a positive Coulomb  
225 stress change of 1 MPa or more to compare with the aftershock zone area (Figure 4). The results  
226 of our Coulomb stress change calculations are listed in Table S3.

## 227 **3. Results**

228 We analyze a total number of 12  $M_w \geq 5.4$  California mainshocks (Table 1), with 3 from the  
229 NCEDC double-difference catalog and the rest from the SCEDC waveform relocated catalog.  
230 Most of them are strike-slip events, except for the 1994 Northridge earthquake with a thrust  
231 mechanism and the 1989 Loma Prieta earthquake with an oblique mechanism. We calculate the  
232 ratio of aftershock zone area to mainshock rupture area of each mainshock, often for multiple slip  
233 inversion models (Figure 5). The parameters that we used are summarized in Table S4. We also  
234 list the data types used by each slip model in Figure 5. Strong ground motion data are  
235 predominantly used for Northern California (NC) earthquakes, while various data types are used  
236 for Southern California (SC) earthquakes.

237 We find that aftershock zone areas are within a range of 0.5 to 5.5 times of the mainshock rupture  
238 area (Figure 6). Some earthquakes such as the 1989 Loma Prieta earthquake have consistently  
239 higher ratios, while others such as the 1999 Hector Mine earthquake and the 1994 Landers  
240 earthquake have consistently lower ratios. We explore their potential causes further in the  
241 discussion section. Ratios of the same earthquake estimated from different slip inversion models  
242 can vary widely. For example, the ratio for the Gallovič (2016) model of the South Napa  
243 earthquake is more than 3 times of the ratio for the Wei et al. (2015) model. This is partially  
244 because the Wei et al. (2015) model has a peak slip and slip area that is twice as large as the  
245 Gallovič (2016) model. The two slip models also assume significantly different fault planes. Since  
246 only earthquakes within 2km of the fault planes are included as potential aftershocks, the  
247 aftershock zone area estimated for Wei's model is smaller than that for Gallovič's model. Our  
248 results also show a similar pattern between the ratios estimated from the ANSS and relocated  
249 earthquake catalogs. Table 2 shows that both types of catalogs have almost identical average ratios,  
250 but the ANSS catalog has larger variance. We also note that the ratios for Brawley and Elmore  
251 Ranch earthquakes differ by a factor of 2 across the relocated and ANSS catalogs. The similar  
252 ratios estimated from different catalogs demonstrate that aftershock zone area is a macroscopic

253 source feature that is not sensitive to the differences of earthquake locations in catalogs. We do  
254 not observe a clear correlation between moment magnitudes and aftershock ratios either (Figure  
255 S3).

### 256 *Early Aftershock Zone*

257 Above results are based on the entire aftershock duration. Since different aftershock generation  
258 mechanisms could affect the long-term aftershock evolution, we also measure ratios using only  
259 early aftershocks to exclude postseismic deformation if existed. The early aftershock window is  
260 set as 1-day after the mainshock (Kanamori, 1977) and the results are shown in Figure 7. Since the  
261  $T_a/T$  term is close to 0 in our study, every single earthquake in each cell after the mainshock would  
262 be significant in the output beta value, which could lead to biased results unless an accurate  
263 background rate and complete early aftershock catalog are guaranteed. Hence, only the off-fault  
264 distance, gap size and  $M_c$  are used to determine which aftershocks to include in the analysis.  
265 Generally, the ratios for the 1-day duration are smaller than or equal to those for the entire  
266 aftershock duration. But the range of median ratios (0.5-3.7) is comparable to the range for the  
267 entire aftershock duration (0.5-5.5). The statistics of the early aftershock ratios are shown in Table  
268 2.

## 269 **4. Discussion**

### 270 *Static Stress Change*

271 If aftershocks are primarily triggered by the Coulomb stress change, they should occur within the  
272 area with the positive Coulomb stress change. Hence, we compare the Coulomb stress change area  
273 and the aftershock zone area of each mainshock (Figure 3). We find that the Coulomb stress change  
274 area shows a positive correlation with the aftershock zone area (Figure 8), which may support the  
275 hypothesis of static stress change being a triggering mechanism for aftershocks. However, this

276 correlation does not necessarily mean causation. For example, the correlation may indicate that  
277 both static stress changes and aftershock areas are related to certain mainshock source parameters.  
278 The correlation between the Coulomb stress change and the aftershock zone area is not an ideal  
279 linear trend either, and the discrepancies may be due to the uncertainty of coseismic slip model  
280 and the inclusion of other aftershock triggering mechanisms. In particular, the Loma Prieta  
281 aftershock zone area appears to be an outlier, as its aftershock zone area is much larger than that  
282 of the other earthquakes given its relatively small Coulomb stress change area. We also show the  
283 ratio of Coulomb stress area to aftershock area with magnitude (Figure 9), and the results are  
284 inconclusive, with either a slight increase or no change in ratio with magnitude depending on the  
285 fitting method used.

### 286 *Afterslip*

287 As Coulomb stress change cannot satisfactorily explain the large aftershock zone area of the Loma  
288 Prieta mainshock, an alternative mechanism for aftershock generation is afterslip following the  
289 mainshock. The variation of geologic conditions in California results in different amounts of  
290 afterslip for each earthquake. The central part of the San Andreas Fault exhibits large amounts of  
291 aseismic creep (Khoshmanesh and Shirzaei, 2018), whereas the southern portion is locked with  
292 significant slip deficit (Fialko, 2006). Though the underlying reason is not well known, some  
293 studies suggest that it might be due to the presence of serpentinite at creeping faults in Northern  
294 and Central California (Moore and Rymer, 2007). Studies have shown that the Loma Prieta  
295 earthquake has afterslip extending around 40-60km towards the southeast along the San Andreas  
296 fault (Behr et al., 1990, Pollitz et al., 1998). The shallow afterslip (above 15km depth) was found  
297 to have most likely occurred on the Loma Prieta fault (Bürgmann et al., 1997). Although the  
298 afterslip was found to be relatively small (less than 1 cm over 4 months), the afterslip area roughly  
299 corresponds to the aftershock zone area in our analysis, which extends southwards for 60 km from

300 the mainshock rupture in a shallow region above 15 km depth. Hence, we argue that the afterslip  
301 should account for the large aftershock zone area of Loma Prieta.

302 Afterslip can occur in the surrounding region loaded by mainshock rupture and transfer stresses  
303 on faults that promote the generation of aftershocks. It is unfeasible to quantitatively evaluate the  
304 contribution by Coulomb stress change and other mechanisms without detailed rupture simulation  
305 based on realistic parameters. For mainshocks with observed afterslip, a combination of the static  
306 stress change and afterslip instead of the Coulomb stress change alone could contribute to the  
307 positive correlation between the Coulomb stress change area and the aftershock zone area. By  
308 comparing the ratios from using both entire aftershock duration (Figure 6) and early aftershocks  
309 (Figure 7), we observe that the long-term aftershock duration results in relatively larger ratio for  
310 the South Napa, Loma Prieta, Brawley, Joshua Tree and North Palm Springs earthquakes. The  
311 larger ratio could be explained by expanding aftershock zones with time caused by postseismic  
312 deformation process. In contrast, similar range of aftershock ratios for the other earthquakes  
313 support that Coulomb stress change caused by the mainshock rupture plays an important role in  
314 aftershock distribution.

315 We also search for published work on postseismic slip following the studied mainshocks, and  
316 seven earthquakes have resolved postseismic slip model (Table S5). For most earthquakes  
317 analyzed in the table, the afterslip distribution is similar in extent to our aftershock zone area  
318 though their depths may be different, which is consistent with emerging evidences that afterslip  
319 could affect the long-term aftershock evolution (Perfettini et al., 2018). To better understand the  
320 outlier mainshocks, we could potentially use afterslip models to measure the stress change caused  
321 by afterslip, similar to that of Pefettini and Avouac (2004; 2007), to ascertain if it correlates better  
322 with their aftershock zone areas. This exceeds the scope of this study and could be a potential work  
323 in future with more available afterslip models.

## 324 *Uncertainty and Limitations*

325 The measurement uncertainties in our calculations include the (1) earthquakes locations, (2) the  
326 calculation of  $M_c$ , (3) the assumption of threshold  $\beta$  value, (4) the upper limit of the grid and gap  
327 size, (5) slip inversion results, and (6) the assumption that the fault plane extends in roughly the  
328 same plane outside of the mainshock rupture area. We examine the uncertainty of earthquake  
329 locations for the Parkfield mainshock using the Ji (2004) model. We use location uncertainties of  
330 0.5km, 1km and 2km to randomly vary the locations of all the aftershocks. We generate 10,000  
331 synthetic distributions of aftershocks and find the standard deviations of aftershock zone areas are  
332 0.09, 0.12 and 0.15 respectively, which is about 4.8 to 7.8% of the mean value. As the location  
333 uncertainties for most earthquakes are smaller than 2km, we believe that the location uncertainty  
334 will not greatly affect the ratios.

335 We calculate  $M_c$  before and after the mainshock and remove earthquakes below  $M_c$ . Though this  
336 procedure ensures that the seismicity change is not biased by the incomplete catalog, it also  
337 removes earthquakes from consideration, which may cause the calculated aftershock zone area to  
338 be smaller than the real aftershock zone area. To estimate the impact of removing earthquakes  
339 below  $M_c$ , we calculate the aftershock zone areas of the Brawley and El Mayor-Cucapah  
340 mainshocks using the Quake Template Matching (QTM) Catalog for Southern California (Ross et  
341 al., 2019) that has a much lower  $M_c$  due to the new detections. The ratios of aftershock zone areas  
342 to mainshock rupture areas estimated from this catalog are larger than that calculated from the  
343 relocated SCEDC catalog (Table S6, Figure S4). However, they are still within the range of ratios  
344 (0.5-5) obtained for all the mainshocks.

345 We limit the calculation of the aftershock zone area by setting a threshold  $\beta$  value of 2. A threshold  
346 value of 2 indicates 95% significance of increase in seismicity when we normalize the  $\beta$  value by  
347 its standard deviation. The assumption behind the calculation of standard deviation is that each

348 earthquake is an independent event and the probability of an earthquake occurring at any given  
349 time is equal. This may not be a valid assumption for earthquakes as the probability of having  
350 earthquakes after a mainshock is much higher than before the mainshock, but all metrics for  
351 determining aftershock zone area necessarily contain arbitrariness.

352 We also set an upper limit of the spatial grid and gap to terminate aftershock zone, which may  
353 violate the observation of the so-called “global aftershock zone” (Parsons and Geist, 2014; Johnson  
354 and Bürgmann, 2016). Among our investigated mainshocks, we noticed an increase of  
355 microearthquakes within the Geysers geothermal region following the 2014 Napa earthquake  
356 (Figure 2), likely triggered by the passing seismic waves (Meng et al., 2014). More recently, Ross  
357 et al. (2019) suggested that the 2010 El Mayor-Cucapah earthquake widely triggered events in  
358 Southern California. Hence, we are referring to the traditional aftershock zone in this study, where  
359 various triggering mechanisms are comparable.

360 As shown by the large variations of ratios for different slip models, slip inversion results probably  
361 contribute to the largest uncertainty in this study. The estimation of ratios can also be affected by  
362 the geometry and orientation of the fault planes as well as the areas enclosed by the slip contours.

### 363 ***Other Results***

364 Studies have shown that aftershocks tend to be concentrated around the boundary of the mainshock  
365 rupture zone, with a deficit in the center regions of higher slip (Mendoza and Hartzell, 1988; Dietz  
366 and Ellsworth, 1990, Wetzler et al., 2018). This is because most of the strain in the regions of  
367 higher slip are already released during the mainshock and hence these areas are less able to  
368 generate aftershocks. We test this hypothesis using a slightly modified version of the method used  
369 in Wetzler et al 2018. Wetzler et al calculated the distances of aftershocks from the slip contours  
370 of several earthquakes, normalized by the radius of a circle that has an area equal to the area  
371 enclosed by the slip contour. As many of our slip contours are elongated, we change the



372 normalization constant to the minor axis of an ellipse fitted to the slip contours (Wijewickrema  
373 and Papliński, 2004), as shown in Figure 10. The distances are then calculated from the closest  
374 slip contour (if there are multiple parts) and normalized by the minor axis of the ellipse fitted to  
375 that slip contour. Negative distances refer to distances of aftershocks inside the slip contour while  
376 positive distances refer to distances of aftershocks outside the slip contour. We use this method to  
377 analyze one slip model from each earthquake (list of models in Table S7). We find that most of  
378 the aftershocks are located near the slip contours, within a distance of -0.25 to 0.25 the slip  
379 contours. Compared to the results obtained by Wetzler et al. (2018), we find more earthquakes  
380 located between 0.5 to 1 distance inside the slip contours (Figure 11), probably because we use the  
381 minor axis of an ellipse as the normalization constant. But our results still support the notion that  
382 there is a deficit of earthquakes in the central regions of the largest slip.

## 383 **5. Conclusion**

384 By analyzing 12 mainshocks ( $M_w \geq 5.4$ ) in California, we find that the ratios of aftershock zone  
385 areas to mainshock rupture areas lie within a range of 0.5 to 5.5, with most values larger than 1.  
386 The ratios are smaller for a short aftershock duration of 1 day, ranging from 0.5 to 3.7. Our results  
387 suggest that aftershock zone areas can generally be used to approximate mainshock rupture areas  
388 for both short and long aftershock durations. Using either the relocated catalog or the ANSS  
389 catalog leads to similar patterns of the aftershock zone area. Our results also show that Coulomb  
390 stress change exhibit a positive correlation with aftershock zone area. Afterslip distribution is  
391 similar in extent to our aftershock zone area for several earthquakes. Therefore, using a  
392 combination of different mechanisms may be necessary to fully understand the characteristics of  
393 the spatial and temporal distribution of aftershocks.

## 394 **Data and Resources**

395 Slip inversion data was downloaded from the SRCMOD website at <http://equake-rc.info>.  
396 Earthquake catalogs were obtained from the NCEDC ([www.ncedc.org](http://www.ncedc.org)) and SCEDC  
397 (<http://scedc.caltech.edu>) websites and the catalog by Dr. Felix Waldhauser  
398 (<https://www.ldeo.columbia.edu/~felixw/NCAeqDD/>), version NCAeqDD.v201112.1. Coulomb  
399 3 MATLAB codes were downloaded from the USGS website  
400 (<https://earthquake.usgs.gov/research/software/coulomb/>), and open-source MATLAB codes for  
401 calculating  $M_c$  are written by D. Schorlemmer and J. Woessner (2004). The supplementary  
402 material contains additional information about individual earthquakes and results of Coulomb  
403 stress change calculations.

#### 404 Acknowledgements

405 We thank the CN Yang Scholars Program, Nanyang Technological University, and the University  
406 of Michigan for supporting the undergraduate research study of Neo Jing Ci. We would also like  
407 to express appreciation to Carissa Tan Xiwen for reviewing this paper.

#### 408 409 References

- 410  
411 Aron, A., Hardebeck, J. L. (2009). Seismicity Rate Changes along the Central California Coast due to Stress  
412 Changes from the 2003 M 6.5 San Simeon and 2004 M 6.0 Parkfield Earthquakes. *Bulletin of the*  
413 *Seismological Society of America*, Vol. 99, No. 4, 2280-2292, doi: 10.1785/0120080239.  
414 Behr, J., Bilham, R., Bodin, P., Burfoid, R. O., Bürgmann, R. (1990). Aseismic slip on the San Andreas Fault  
415 south of Loma Prieta. *Geophysical Research Letters*, 17, 9, 1445–1448.  
416 Berlardinelli, M. E., Bizzarri, A., Cocco, M. (2003). Earthquake triggering by static and dynamic stress  
417 changes. *Journal of Geophysical Research*, 108, B3, 2135.  
418 Bennett, R. A., Reilinger, R. E., Rodi, W., Li, Y. P., Toksoz, M. N., and Hudnut, K. (1995). Coseismic Fault  
419 Slip Associated with the 1992 M(W)-6.1 Joshua-Tree, California, Earthquake - Implications for the  
420 Joshua-Tree Landers Earthquake Sequence. *Journal of Geophysical Research*, 100, B4, 6443-6461  
421 Beroza, G. C. (1991). Near-Source Modeling of the Loma-Prieta Earthquake - Evidence for Heterogeneous  
422 Slip and Implications for Earthquake Hazard. *Bulletin of the Seismological Society of America*, 81,  
423 5, 1603-1621  
424 Bouchon, M., Durand, V., Marsan, D., Karabulut, H., Schmittbuhl, J. (2013). The long precursory phase of  
425 most large interplate earthquakes. *Nature*, 6, 299-302.  
426 Bowman, J. R., Kisslinger, C. (1984). A Test of Foreshock Occurrence in the Central Aleutian Island Arc.  
427 *Bulletin of the Seismological Society of America*, 74, 1, 181-197.  
428 Bürgmann, R., Segall, P., Lisowski, M., Svarc, J. (1997). Postseismic strain following the 1989 Loma Prieta  
429 earthquake from GPS and levelling measurements. *Journal of Geophysical Research*, 102, B3, 4933-  
430 4955.

431 Cattania, C., Hainzl, S., Wang, L., Enescu, B., Roth, F. (2015). Aftershock triggering by postseismic stresses:  
432 A study based on Coulomb rate-and-state models. *Journal of Geophysical Research*, 120, 2388-2407,  
433 doi:10.1002/2014JB011500.

434 Cotton, F., and Campillo. M. (1995). Frequency-Domain Inversion of Strong Motions - Application to the  
435 1992 Landers Earthquake. *Journal of Geophysical Research*, 100 (B3):3961-3975.

436 Custodio, S., Liu, P. C., and Archuleta, R. J. (2005). The 2004 Mw 6.0 Parkfield, California, earthquake:  
437 Inversion of near-source ground motion using multiple data sets. *Geophysical Research Letters*, 32  
438 (23).

439 Das, S. and Henry, C. (2003). Spatial Relation between Main Earthquake Slip and its Aftershock Distribution.  
440 *Reviews of Geophysics*, 41(3), 1013, doi: 10.1029/2002RG000119, 2003.

441 Diao, F., Xiong, X., Wang, R., Zheng, Y., Walter, T. R., Weng, H., Li, J. (2013). Overlapping post-seismic  
442 deformation processes: afterslip and viscoelastic relaxation following the 2011 Mw 9.0 Tohoku  
443 (Japan) earthquake. *Geophysical Journal International*, 196, 1, 218–  
444 229, <https://doi.org/10.1093/gji/ggt376>

445 Dietz, L. D. and Ellsworth, W. L. (1990). The October 17, 1989, Loma Prieta, California, earthquake and  
446 its aftershocks: Geometry of the sequence from high-resolution locations. *Geophysical Research  
447 Letters*, 17, 9, 1417-1420.

448 Dreger, D. S., Gee, L., Lombard, P., Murray, M. H., and Romanowicz, B. (2005). Rapid finite-source analysis  
449 and near-fault strong ground motions: Application to the 2003 M-w 6.5 San Simeon and 2004 Mw  
450 6.0 Parkfield earthquakes. *Seismological Research Letters*, 76 (1):40-48.

451 Dodge, D. A., Beroza, G. C., Ellsworth, W. L. (1995). Foreshock sequence of the 1992 Landers, California,  
452 earthquake and its implications for earthquake nucleation. *Journal of Geophysical Research*, 100, B7,  
453 9865-9880.

454 Ebel, J.E and Chambers, D.W (2016). Using the locations of  $M \geq 4$  earthquakes to delineate the extents of the  
455 ruptures of past major earthquakes. *Geophysical Journal International*, 207, 862–875, doi:  
456 10.1093/gji/ggw312.

457 Emolo, A., and Zollo, A. (2005). Kinematic Source Parameters for the 1989 Loma Prieta Earthquake from the  
458 Nonlinear Inversion of Accelerograms. *Bulletin of the Seismological Society of America*, 95, 3, 981–  
459 994.

460 Fan, W., and Shearer, P. M. (2016). Local near instantaneously dynamically triggered aftershocks of large  
461 earthquakes. *Science*, 353, 6304, 1133-1136.

462 Fialko, Y. (2006). Interseismic strain accumulation and the earthquake potential on the southern San Andreas  
463 fault system. *Nature*, 441, 968-971, doi:10.1038/nature04797.

464 Freed, A. M. (2007). Afterslip (and only afterslip) following the 2004 Parkfield, California, earthquake.  
465 *Geophysical Research Letters*, 34, L06312, doi:10.1029/2006GL029155.

466 Gallovič, F. (2016). Modeling velocity recordings of the Mw6.0 South Napa, California, earthquake: unilateral  
467 event with weak high-frequency directivity. *Seismological Research Letters*, 87, 2-14.

468 Gulia, L. and Wiemer, S. (2019). Real-time discrimination of earthquake foreshocks and aftershocks. *Nature*,  
469 574, pp. 193-200.

470 Hardebeck, J. L., Nazareth, J. J., Hauksson, E. (1998). The static stress change triggering model: Constraints  
471 from two southern California aftershock sequence. *Journal of Geophysical Research*, 103, B10,  
472 24,427-24,437.

473 Hartzell, S. (1989). Comparison of Seismic Waveform Inversion Results for the Rupture History of a Finite  
474 Fault - Application to the 1986 North Palm-Springs, California, Earthquake. *Journal of Geophysical  
475 Research*, 94 (B6):7515-7534.

476 Hartzell, S. H., and Iida, M. (1990). Source complexity of the 1987 Whittier Narrows, California, earthquake  
477 from the inversion of strong motion records. *Journal of Geophysical Research*, 95 (8):12,475-12,485.

478 Hauksson, E., Jones, L. M., and Hutton, K. (2002). The 1999 Mw 7.1 Hector Mine, California, Earthquake  
479 Sequence: Complex Conjugate Strike-Slip Faulting. *Bulletin of Seismological Society of America*,  
480 92, 4, 1154-1170.

481 Hauksson, E., Yang, W., Shearer, P. M. (2012). Waveform Relocated Earthquake Catalog for Southern  
482 California (1981 to June 2011). *Bulletin of the Seismological Society America*, 102, 5, 2239-2244.

483 Hernandez, B., Cotton, F., and M. Campillo. (1999). Contribution of radar interferometry to a two-step  
484 inversion of the kinematic process of the 1992 Landers earthquake. *Journal of Geophysical  
485 Research*, 104 (B6):13083-13099.

486 Ji, C. (2004). Slip history the 2004 (Mw 5.9) Parkfield Earthquake (Single-Plane Model). Retrieved from  
487 [http://www.tectonics.caltech.edu/slip\\_history/2004\\_ca/parkfield2.html](http://www.tectonics.caltech.edu/slip_history/2004_ca/parkfield2.html), last accessed Mar 26, 2019.

488 Johnson, C., W., and Bürgmann, R. (2016). Delayed dynamic triggering: Local seismicity leading up to three  
489 remote  $M \geq 6$  aftershocks of the 11 April 2012 M8.6 Indian Ocean earthquake. *Journal of Geophysical*  
490 *Research*, 121, 134-151, doi:10.1002/2015JB012243.

491 Jonsson, S., Zebker, H., Segall, P., and Amelung, F. (2002). Fault slip distribution of the 1999 Mw 7.1 Hector  
492 Mine, California, earthquake, estimated from satellite radar and GPS measurements. *Bull. Seis. Soc.*  
493 *Am* 92 (4):1377-1389.

494 Kanamori, H. (1977). The Energy Release in Great Earthquakes. *Journal of Geophysical Research*, 82, 20,  
495 2981-2987.

496 Kaverina, A., Dreger, D., and Price, E. (2002). The combined inversion of seismic and geodetic data for the  
497 source process of the 16 October 1999 Mw 7.1 Hector Mine, California, earthquake. *Bulletin of the*  
498 *Seismological Society of America*, 92 (4):1266-1280.

499 Kelleher (1972). Rupture Zones of Large South American Earthquakes and Some Predictions. *Journal of*  
500 *Geophysical Research*, 77, 11, 2087-2103.

501 Khoshmanesh, M. and Shirzaei, M. (2018). Episodic creep events on the San Andreas Fault caused by pore  
502 pressure variations. *Nature, Geoscience*, volume 11, 610–614.

503 Kilb, D., Gomberg, J., Bodin, P. (2000). Triggering of earthquake aftershocks by dynamic stresses. *Nature*,  
504 408, 570-574.

505 Kilb, D., Gomberg, J., Bodin, P. (2002). Aftershock triggering by complete Coulomb stress changes. *Journal*  
506 *of Geophysical Research*, 107, B4, ESE 2-1-ESE 2-14.

507 King, G.C.P., Stein, R.S., Lin, J. (1994). Static Stress Changes and the Triggering of Earthquakes. *Bulletin of*  
508 *Seismological Society of America*, Vol. 84, No. 3, pp 935-953.

509 Knopoff, L., Kagan, Y., Knopoff, R. (1982). b Values for Foreshocks and Aftershocks in Real and Simulated  
510 Earthquake Sequences. *Bulletin of the Seismological Society of America*, 72, 5, 1663-1676.

511 Larsen, S., Reilinger, R., Neugebauer, H., and Strange, W., (1992). Global Positioning System Measurements  
512 of Deformations Associated with the 1987 Superstition Hills Earthquake - Evidence for Conjugate  
513 Faulting. *Journal of Geophysical Research*, 97 (B4):4885-4902.

514 Ma, K. F., Chan, C. H., Stein, R. S. (2005). Response of seismicity to Coulomb stress triggers and shadows of  
515 the 1999 Mw = 7.6 Chi-Chi, Taiwan, earthquake. *Journal of Geophysical Research*, 110, B05S19,  
516 doi:10.1029/2004JB003389.

517 Marsan, D. and Lengliné, O. (2010). A new estimation of the decay of aftershock density with distance to the  
518 mainshock. *Journal of Geophysical Research*, 115, B09302.

519 Matthews, M. V., Reasenber, P. A. (1988). Statistical Methods for Investigating Quiescence and Other  
520 Temporal Seismicity Patterns. *Pure and Applied Geophysics*, 126, 2-4, 357-372.

521 Meade, B. J., DeVries, P. M. R., Faller, J., Viegas, F., & Wattenberg, M. (2017). What is better than Coulomb  
522 failure stress? A ranking of scalar static stress triggering mechanisms from 10 mainshock-aftershock  
523 pairs. *Geophysical Research Letters*, 44, 11,409–11,416, doi: <https://doi.org/10.1002/2017GL075875>.

524 Mendoza, C., and Hartzell, S. H., (1988). Inversion for slip distribution using teleseismic P waveforms; North  
525 Palm Springs, Borah Peak, and Michoacan earthquakes. *Bulletin of the Seismological Society of*  
526 *America*, 78 (3):1092-1111.

527 Mendoza, C. and Hartzell, S. (2013). Finite-fault source inversion using teleseismic P waves: Simple  
528 parameterization and rapid analysis. *Bulletin of the Seismological Society of America*, 103(2A), 834-  
529 844.

530 Meng, X., Peng, Z. (2016). Increasing lengths of aftershock zones with depths of moderate-size earthquakes  
531 on the San Jacinto Fault suggests triggering of deep creep in the middle crust. *Geophysical Journal*  
532 *International*, 204, 250-261, doi: 10.1093/gji/ggv445.

533 Meng, X., Peng, Z., Aiken, C., Kilb, D. (2014). Dynamically triggered earthquakes in the Geysers region  
534 following the 2014 M6.0 South Napa earthquake, Eos AGU Fall Meeting.

535 Mignan, A., J. Woessner (2012), Estimating the magnitude of completeness in earthquake catalogs,  
536 Community Online Resource for Statistical Seismicity Analysis, doi:10.5078/corssa-00180805.  
537 Available at <http://www.corssa.org>.

538 Moore, D. E., Rymer, M. J. (2007). Talc-bearing serpentinite and the creeping section of San Andreas Fault.  
539 *Nature*, 448, 795-797.

540 NCEDC (2014), Northern California Earthquake Data Center. UC Berkeley Seismological Laboratory.  
541 Dataset. doi:10.7932/NCEDC.

542 Parsons, T. (2002). Global Omori law decay of triggered earthquakes: Large aftershocks outside the classical  
543 aftershock zone. *Journal of Geophysical Research*, 107, B9, 2199, doi: 10.1029/2001JB000646.

544 Parsons, T., Geist, E. L. (2014). The 2010–2014.3 global earthquake rate increase. *Geophysical Research*  
545 *Letters*, 41, 13, 4479-4485.

546 Perfettini, H., Avouac, J. P. (2007). Modeling afterslip and aftershocks following the 1992 Landers earthquake.  
547 *Journal of Geophysical Research*, 112, B07409, doi:10.1029/2006JB004399.

548 Perfettini, H., Avouac, J. P., Ruegg, J. C. (2005). Geodetic displacements and aftershocks following the 2001  
549 Mw = 8.4 Peru earthquake: Implications for the mechanics of the earthquake cycle along subduction  
550 zones. *Journal of Geophysical Research*, 110, B09404, doi:10.1029/2004JB003522

551 Pollitz, F. F., Bürgmann, R., Segall, P. (1998). Joint estimation of afterslip rate and postseismic relaxation  
552 following the 1989 Loma Prieta earthquake. *Journal of Geophysical Research*, 103, B11, 26,975-  
553 26,992.

554 Ross, Z.E., Trugman, D.T., Hauksson, E., and P.M. Shearer (2019). Searching for Hidden Earthquakes in  
555 Southern California. *Science*, 364, 6442, 767-771.

556 Savage, J. C., Svarc, J. L., Yu, S. B. (2007). Postseismic relaxation and aftershocks. *Journal of Geophysical*  
557 *Research*, 112, B06406, doi: 10.1029/2006JB004584.

558 SCEDC (2013): Southern California Earthquake Center. Caltech Dataset. doi:10.7909/C3WD3xH1.

559 Sykes, L. R. (1971). Aftershock Zones of Great Earthquakes, Seismicity Gaps, and Earthquake Prediction for  
560 Alaska and the Aleutians. *Journal of Geophysical Research*, 76(32), 8021-8041.

561 Tajima, F., Kanamori, H. (1985). Global survey of aftershock zone area expansion patterns. *Physics of the*  
562 *Earth and Planetary Interiors*, 40, 77-134.

563 Toda, S., Stein, R. S., Reasenber, P. A., Dieterich, J. H., Yoshida, A. (1998). Stress transferred by the 1995  
564 Mw -- 6.9 Kobe, Japan, shock: Effect on aftershocks and future earthquake probabilities. *Journal of*  
565 *Geophysical Research*, 103, B10, 24 543-24565.

566 Toda, S., Stein, R. S., Lin, J. (2011). Widespread seismicity excitation throughout central Japan following the  
567 2011 M=9.0 Tohoku earthquake and its interpretation by Coulomb stress transfer. *Geophysical*  
568 *Research Letters*, 38, L00G03, doi:10.1029/2011GL047834.

569 USGS (2019). ANSS Comprehensive Earthquake Catalog (ComCat). Retrieved from  
570 <https://earthquake.usgs.gov/earthquakes/search/>

571 Utsu, T. (1970). Aftershocks and Earthquake Statistics (1): Some Parameters Which Characterize an  
572 Aftershock Sequence and Their Interrelations. *Journal of the Faculty of Science, Hokkaido University.*  
573 *Series 7, Geophysics*, 3(3): 129-195.

574 Van der Elst, N. J., and Brodsky, E. E. (2010). Connecting near-field and far-field earthquake triggering to  
575 dynamic strain. *Journal of Geophysical Research*, 115, B07311.

576 Wald, D. J., T. H. Heaton, and K. W. Hudnut. 1996. The slip history of the 1994 Northridge, California,  
577 earthquake determined from strong-motion, teleseismic, GPS, and leveling data. *Bulletin of the*  
578 *Seismological Society of America*, 86 (1): S49-S70.

579 Wald, D. J., Helmberger, D. V., and Heaton, T. H. (1991). Rupture Model of the 1989 Loma-Prieta Earthquake  
580 from the Inversion of Strong-Motion and Broad-Band Teleseismic Data. *Bulletin of the Seismological*  
581 *Society of America*, 81 (5):1540-1572.

582 Waldhauser, F., Near-real-time double-difference event location using long-term seismic archives, with  
583 application to Northern California, *Bulletin of the Seismological Society of America*, 99, 2736-  
584 2848, doi:10.1785/0120080294, 2009.

585 Waldhauser, F. and D.P. Schaff (2008). Large-scale relocation of two decades of Northern California  
586 seismicity using cross-correlation and double-difference methods, *J. Geophys. Res.*, 113, B08311,  
587 doi:10.1029/2007JB005479.

588 Wei, S., Fielding, E., Leprince, S., Sladen, A., Avouac, J.P., Helmberger, D., Hauksson, E., Chu, R., Simons,  
589 M., Hudnut, K., Herring T., and Briggs, R. (2011). Superficial simplicity of the 2010 El Mayor-  
590 Cucupah earthquake of Baja California in Mexico. *Nature Geoscience*. doi:10.1038/ngeo1213.

591 Wei, S., Helmberger, D. V., Owen, S., Graves, R. W., Hudnut, K. W., and Fielding, E. (2013). Complementary  
592 slip distributions of the largest earthquakes in the 2012 Brawley swarm, Imperial Valley, California.  
593 *Geophysical Research Letters*, 40, 1-6, doi:10.1002/grl.50259.

594 Wei, S., Barbot, S., Graves, R., Lienkaemper, J. J., Wang, T., Hudnut, K., Fu, Y., and Helmberger, D. (2015).  
595 The 2014 Mw 6.1 South Napa Earthquake: A Unilateral Rupture with Shallow Asperity and Rapid  
596 Afterslip. *Seismological Research Letters*, 86(2A), 344-354.

597 Wells, D. L., Coppersmith, K. J. (1994). New Empirical Relationships among Magnitude, Rupture Length,  
598 Rupture Width, Rupture Area, and Surface Displacement. *Bulletin of the Seismological Society of*  
599 *America*, Vol. 84, No. 4., pp 974 – 1002.

600 Wetzler, N., Lay, T., Brodsky, E., Kanamori, H., (2018). Systematic deficiency of aftershocks in areas of high  
601 coseismic slip for large subduction zone earthquakes. *Science Advances*, 4(2) eaao3225, DOI:  
602 10.1126/sciadv.aao3225.  
603 Wijewickrema, S. N. R., Paplinski, A. P. (2004). Principal Component Analysis for the Approximation of a  
604 Fruit as an Ellipse.  
605 Zeng, Y., and Anderson. J. (2000). Evaluation of numerical procedures for simulating near-fault long-period  
606 ground motions using Zeng method. Report 2000/01 to the PEER Utilities Program, available at  
607 <http://peer.berkeley.edu>

### **Full Mailing Addresses of Authors**

Jing Ci Neo

University of Michigan, Ann Arbor. Room 4534F, 1100 North University

Yihe Huang

University of Michigan, Ann Arbor. Room 4534F, 1100 North University

Dongdong Yao

University of Michigan, Ann Arbor. Room 4534F, 1100 North University

Shengji Wei

Earth Observatory of Singapore, 50 Nanyang Avenue, Block N2-01a-15

## List of Tables

**Table 1**  
**Summary of the source properties and ratios of earthquakes.**

Earthquake	Date	Location N/W	Magnitude (Mw)	Depth (km)	Slip Inversion References	Data Sources*	Reloc.	ANSS
South Napa (SN)	2014/08/24	38.22/122.31	6.10	11.0	Wei et al (2015)	SGM	1.04	0.92
			6.07	10.0	Gallovič (2016)	SGM	4.16	3.66
			5.90	8.0	Ji (2004)	SGM, GPS	1.28	2.04
Parkfield (Pf)	2004/09/28	35.82/120.37	6.00	8.3	Dreger et al (2005)	SGM, GPS	2.37	2.70
			6.06	8.3	Custodio et al (2005)	SGM	2.36	2.18
			6.98	17.6	Zeng and Anderson (2000)	SGM	5.38	4.54
Loma Prieta (LP)	1989/10/18	37.04/121.88	6.94	17.6	Wald et al (1991)	SGM, TELE	4.19	3.53
			6.96	17.6	Beroza (1991)	SGM	3.82	5.23
			6.91	17.6	Emolo and Zollo (2005)	SGM	3.40	4.69
Brawley Swarm (BS)	2012/08/26	33.02/115.54	5.45	6.4	Wei et al (2013)	SGM, GPS	0.82	2.29
El-Mayor- Cucapah (EMC)	2010/04/04	32.30/115.30	7.35	10.0	Mendoza and Hartzell (2013)	TELE	2.17	2.61
			7.29	5.5	Wei et al (2011)	TELE, SPOT, GPS, INSAR, SAR	1.79	1.74
Hector Mine (HM)	1999/10/16	34.59/116.27	7.24	6.0	Kaverina et al (2002)	SGM, GPS	1.26	1.18
			7.16	15.0	Jonsson et al (2002)	GPS, INSAR	1.49	0.98
			6.71	17.5	Zeng and Anderson (2000)	SGM	2.33	3.01
Northridge (Nr)	1994/01/17	34.21/118.54	6.80	17.5	Wald et al (1996)	SGM, TELE, GPS	1.30	1.88
			6.81	17.5	Hudnut et al (1996)	TRIL, GPS	1.38	1.67
			6.73	17.5	Hartzell et al (1996)	SGM	1.21	1.49
			7.20	7.0	Zeng and Anderson (2000)	SGM	1.15	0.88
Landers (Ld)	1992/06/28	34.20/116.43	7.22	7.0	Hernandez et al (1999)	SGM, GPS	1.80	1.26
			7.29	7.0	Cotton and Campillo (1995)	SGM	1.47	1.15
Joshua Tree (JT)	1992/04/23	34.00/116.32	6.25	12.5	Bennett et al (1995)	TRIL, GPS	2.12	1.96
Elmore Ranch (ER)	1987/11/24	33.08/115.80	6.52	10.0	Larsen et al (1992)	TRIL, GPS	4.30	2.06
Whittier Narrows (WN)	1987/10/01	34.05/118.08	5.89	14.6	Hartzell and Iida (1990)	SGM	1.61	NA
North Palm Springs (NPS)	1986/07/08	34.00/116.57	6.14	11.0	Hartzell (1989)	SGM	0.54	0.79
			6.21	11.0	Mendoza and Hartzell (1988)	TELE	1.87	2.72

\*SGM: Strong ground motion, TELE: Telesismic data, GPS: Global Positioning System, SAR: Synthetic-Aperture Radar, INSAR: Interferometric Synthetic-Aperture Radar, SPOT: Optical imaging from the SPOT-5 satellite.



**Table 2**  
**Statistics of the ratios**

	Entire Duration		1-Day Aftershocks	
	Relocated Catalogs	ANSS Catalog	Relocated Catalogs	ANSS Catalog
Mean	2.18	2.16	1.79	1.79
Variance	1.58	1.90	0.64	1.28
Median	1.80	2.00	1.67	1.73
Mean Absolute Deviation	0.98	1.03	0.67	0.94

## List of Figure Captions

**Figure 1.** Map of mainshock locations in this study. Known faults are specified as dark red lines, and the direction of plate motion is indicated by black arrows.

**Figure 2.** Illustration of how the aftershock zone area of each mainshock is defined using the  $\beta$  values. The diagrams show the fault plane view, with  $\beta$  values of each grid cell calculated from the aftershocks projected on to the fault plane. Aftershocks from the relocated catalogs are used for this figure.

**Figure 3.** Illustration of how aftershock duration is calculated. The horizontal black line is at a  $\beta$  value of 2, and the aftershock duration is taken to be the end of the time window where the  $\beta$  value first dips below the line (indicated by the stars). If the  $\beta$  value never dips below 2, 1 year is used. For example, the aftershock durations for Parkfield and Northridge are the same ( $>1$  year).

**Figure 4.** Depiction of how the coulomb stress change area is calculated. For illustration, a contour is drawn around the boundary of cells with a positive coulomb stress change of  $>1$  MPa or more. The coulomb stress change area is given by the sum of the area of these cells.

**Figure 5.** Plot of the data types used for each slip inversion, where the ratios are calculated using the relocated catalogs. SGM: Strong ground motion; Teleseismic: Teleseismic waveform data; Geodetic: GPS, INSAR.

**Figure 6.** Plot of ratios sorted by earthquake, with the full names of each earthquake in Table 1. The black crosses represent ratios of different slip inversion models for each earthquake, while the red dots represent the median values of the ratios. (Left) NCEDC data is used to calculate the aftershock zone area for the first 3 earthquakes, while SCEDC data is used for the rest of the earthquakes. (Right) ANSS catalog is used. The ratio for the Whittier Narrows (WN) earthquake is not obtained from the ANSS catalog because the data does not yield a robust estimation of the magnitude of completeness.

**Figure 7.** Aftershock ratios calculated from 1-day aftershock durations for both earthquake catalogs.

**Figure 8.** Aftershock zone area vs. Coulomb stress change area.

**Figure 9.** Robust fitting (solid line) and least squares fitting (dashed line) of ratios of Coulomb stress area to aftershock zone area with magnitude.

**Figure 10.** Illustration of how the distances from slip contour are calculated using the Parkfield, Chen Ji et al slip model.

**Figure 11.** Histogram of aftershock distances from slip contours for all earthquakes using the relocated and ANSS catalogs.

## List of Figures

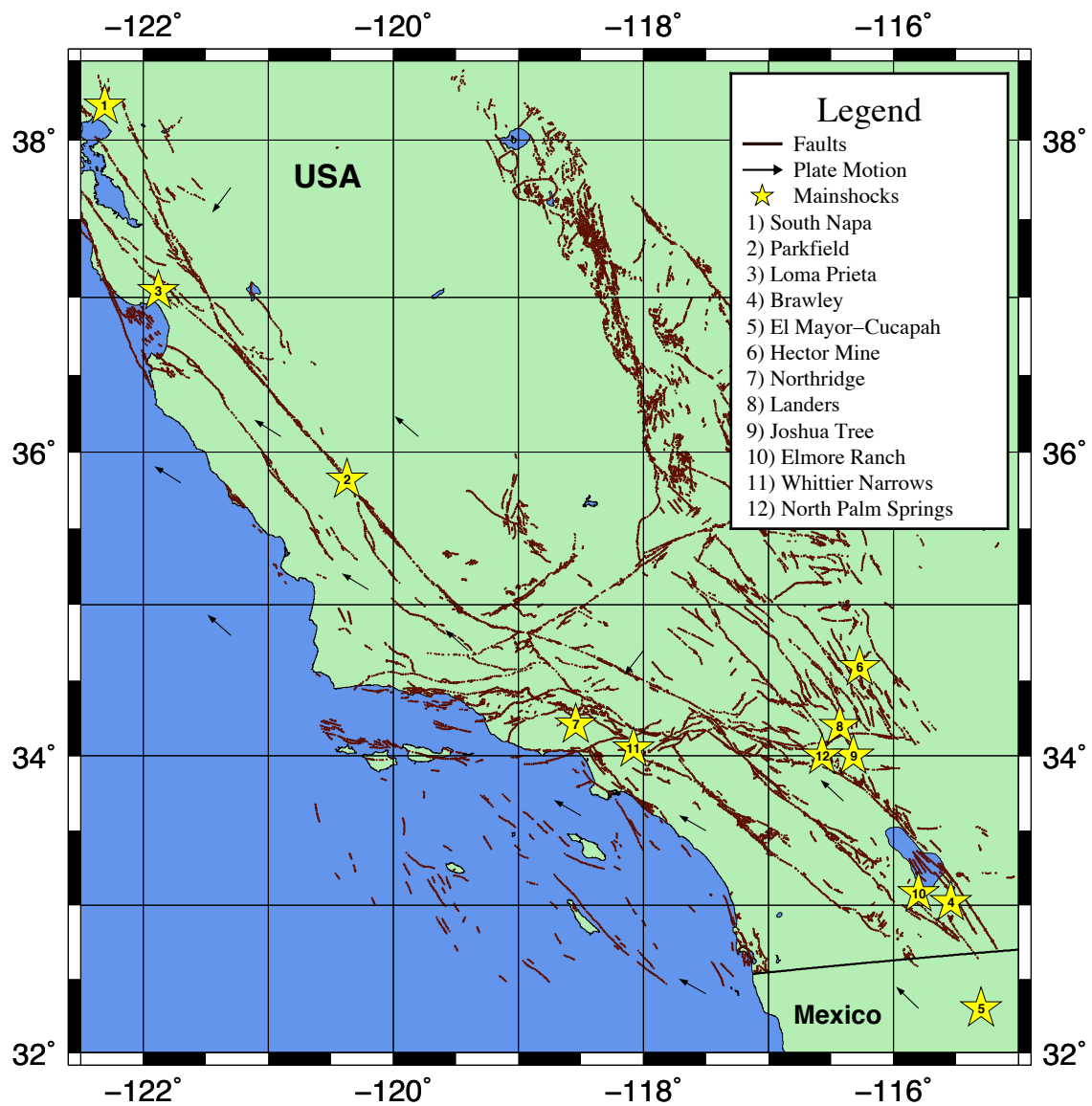


**Figure 1.** Map of mainshock locations in this study. Known faults are specified as dark red lines, and the direction of plate motion is indicated by black arrows.

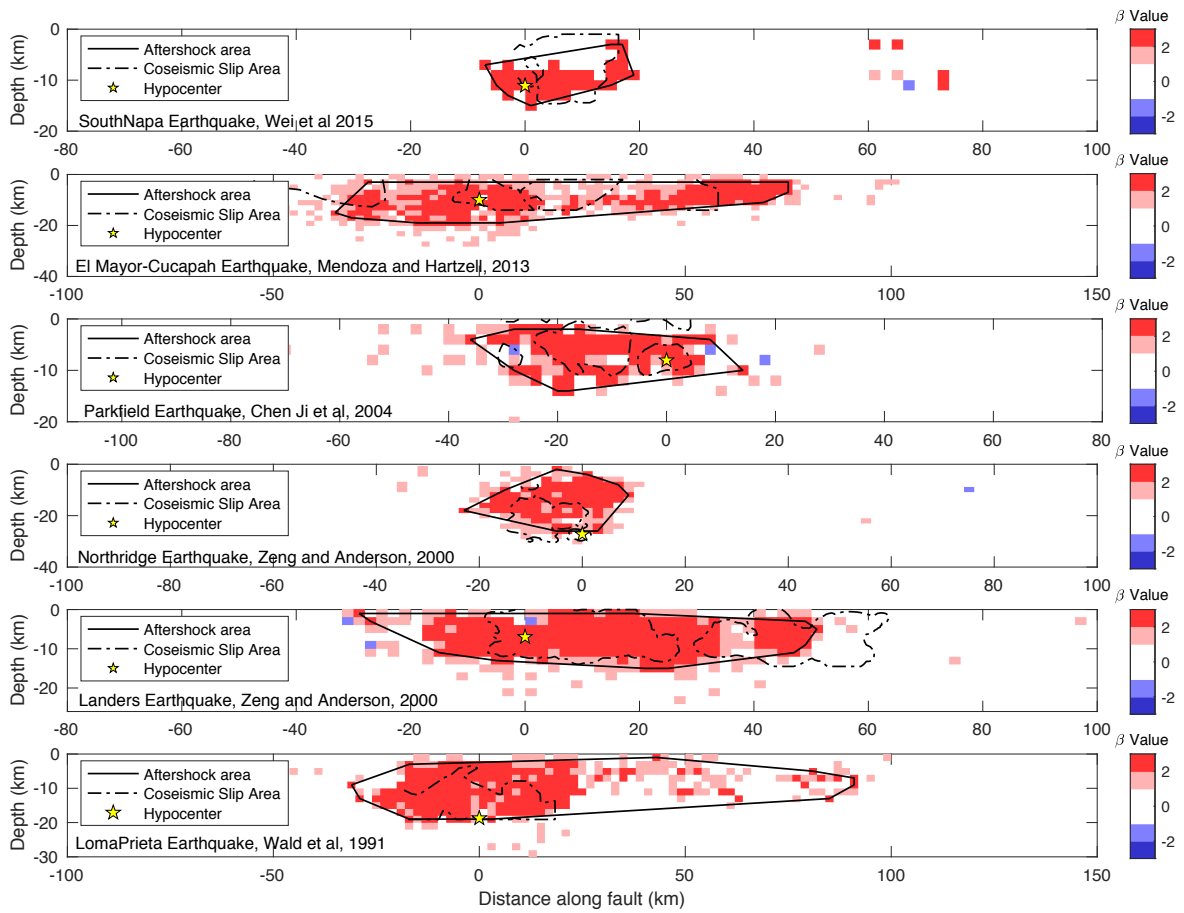


**Figure 2.** Illustration of how the aftershock zone area of each mainshock is defined using the  $\beta$  values. The diagrams show the fault plane view, with  $\beta$  values of each grid cell calculated from the aftershocks projected on to the fault plane. Aftershocks from the relocated catalogs are used for this figure.

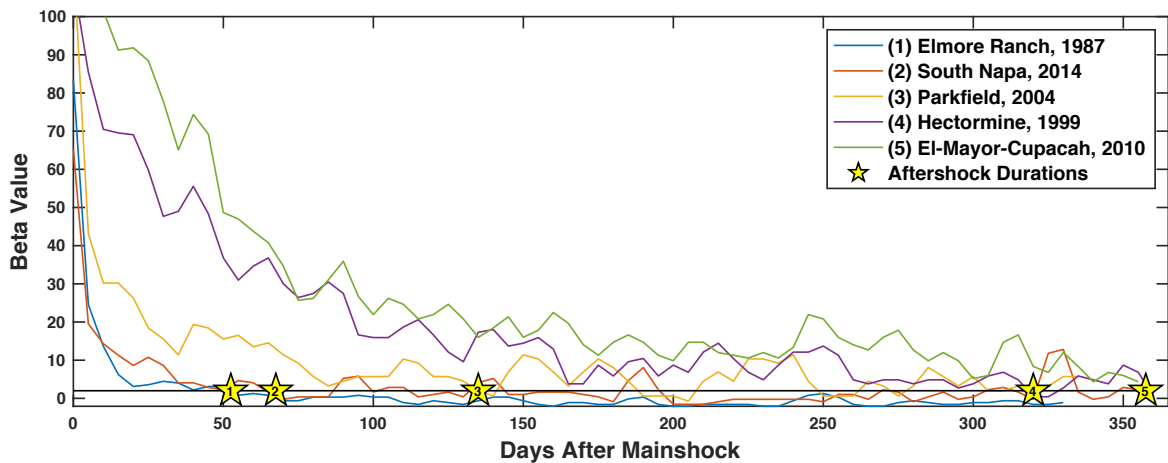


**Figure 3.** Illustration of how aftershock duration is calculated. The horizontal black line is at a  $\beta$  value of 2, and the aftershock duration is taken to be the end of the time window where the  $\beta$  value first dips below the line (indicated by the numbered stars). If the  $\beta$  value never dips below 2, 1 year is used.

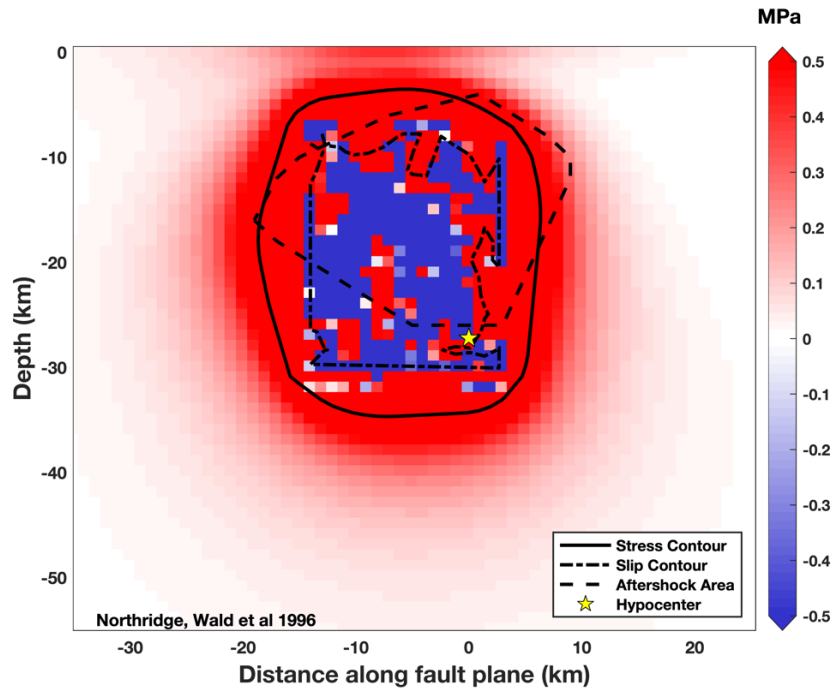


**Figure 4.** Depiction of how the coulomb stress change area is calculated. For illustration, a contour is drawn around the boundary of cells with a positive coulomb stress change of  $>1$  MPa or more. The coulomb stress change area is given by the sum of the area of these cells.

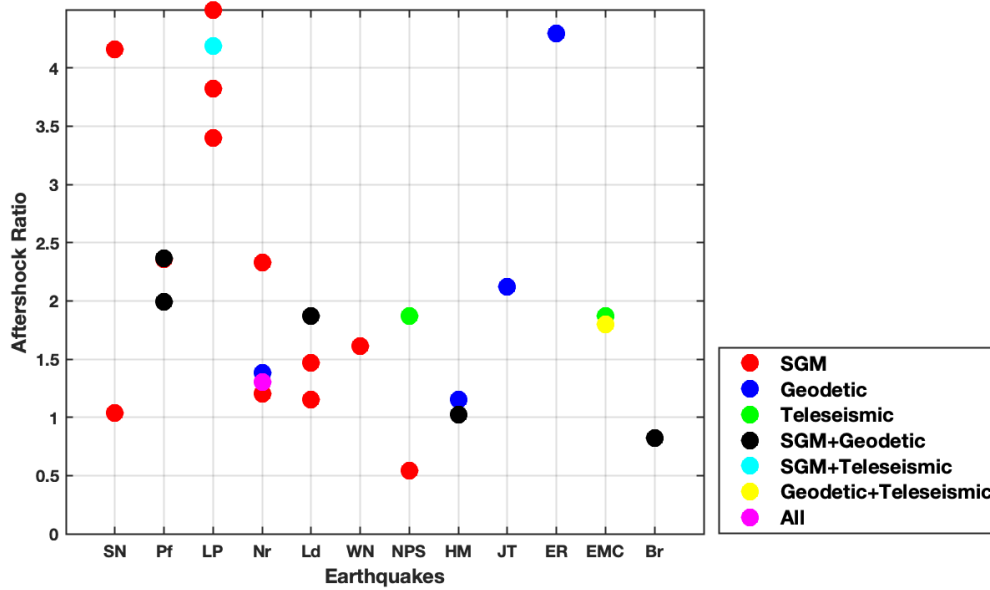


**Figure 5.** Plot of the data types used for each slip inversion, where the ratios are calculated using the relocated catalogs. SGM: Strong ground motion; Teleseismic: Teleseismic waveform data; Geodetic: GPS, INSAR.

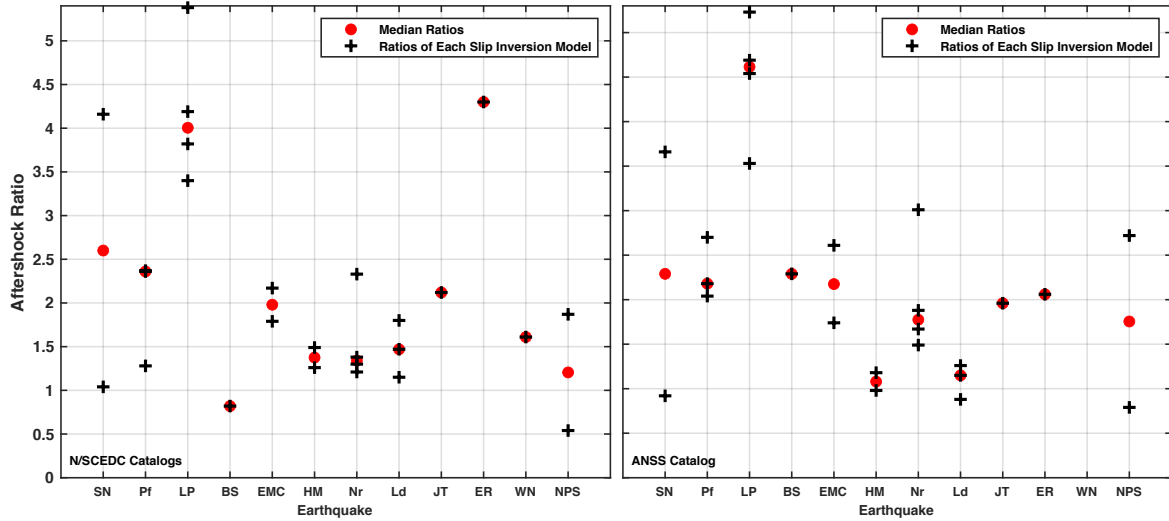


**Figure 6.** Aftershock zone area ratios for different earthquakes using different earthquake catalogs, with the full names of each earthquake in Table 1. The black crosses represent ratios of different slip inversion models for each earthquake, while the red dots represent the median values of the ratios. (Left) NCEDC data is used to calculate the aftershock zone area for the first 3 earthquakes, while SCEDC data is used for the rest of the earthquakes. (Right) ANSS catalog is used. The ratio for the Whittier Narrows (WN) earthquake is not obtained from the ANSS catalog because the data does not yield a robust estimation of the magnitude of completeness.

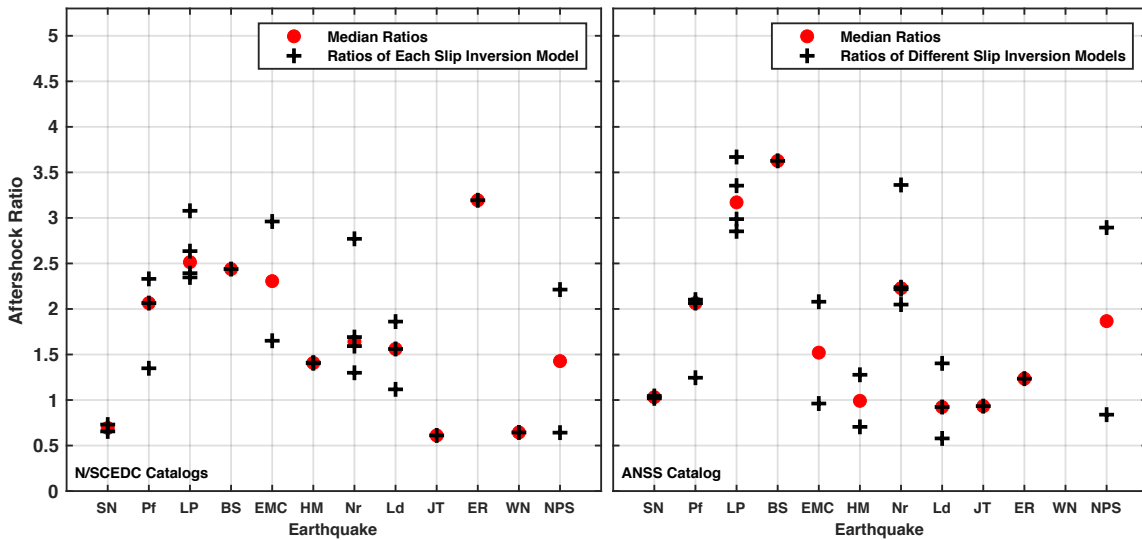


**Figure 7.** Aftershock ratios calculated from 1-day aftershock durations for both earthquake catalogs.

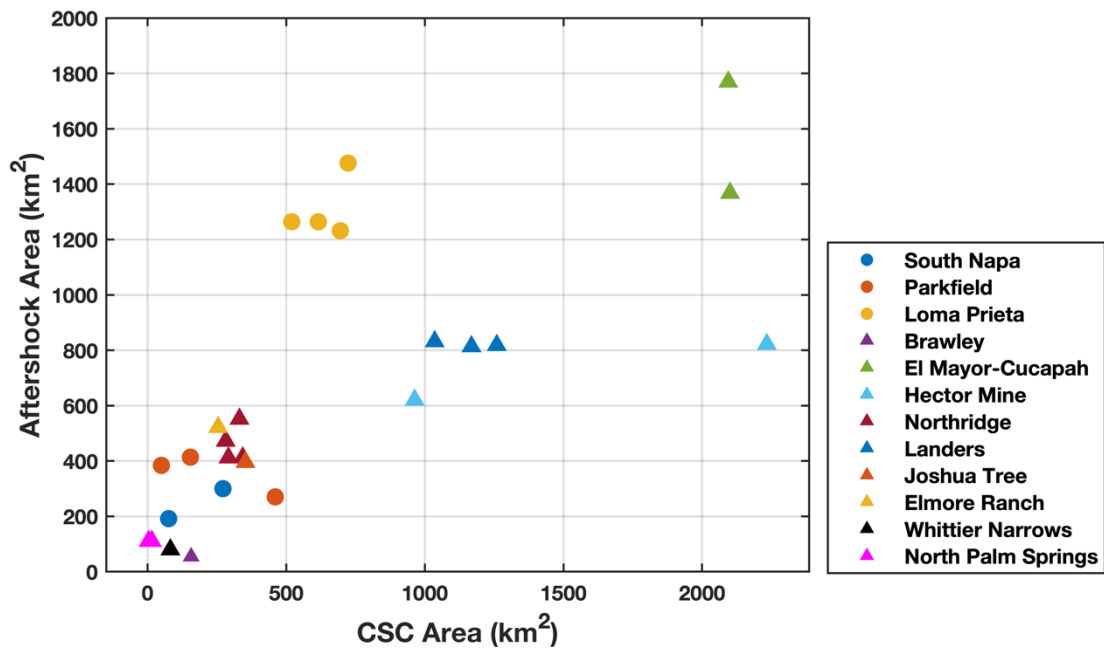


Figure 8. Aftershock zone area vs. Coulomb stress change area.

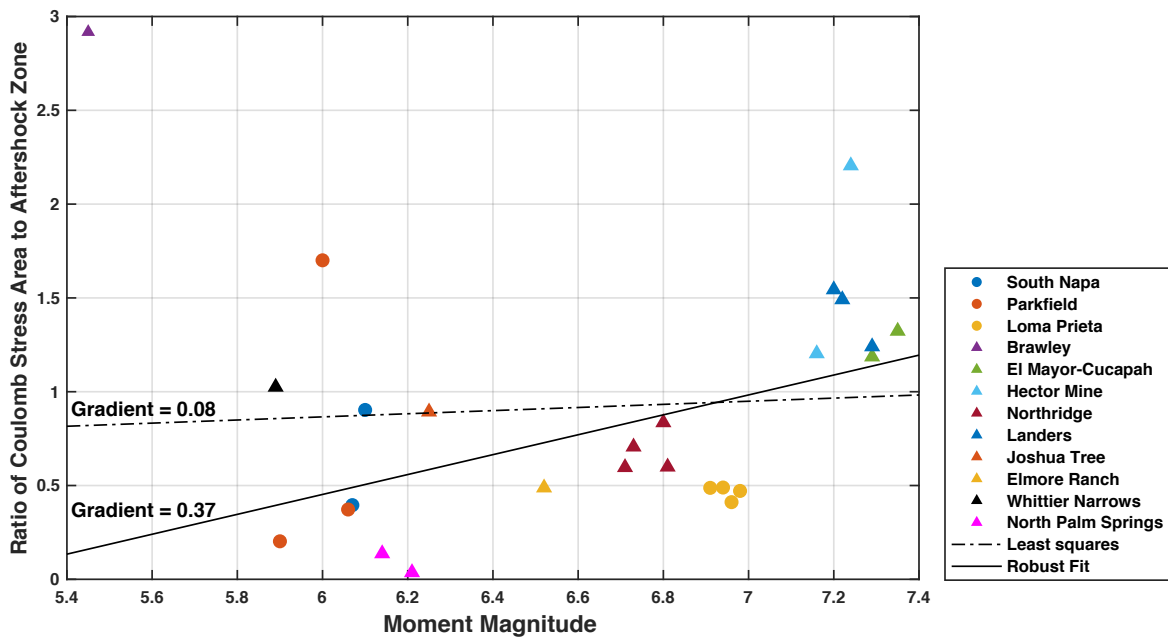
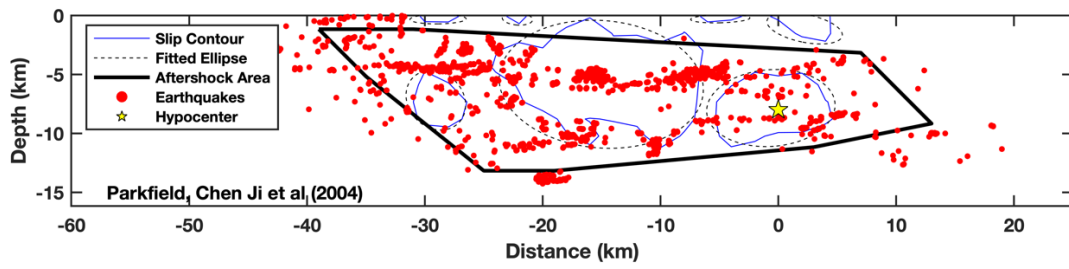
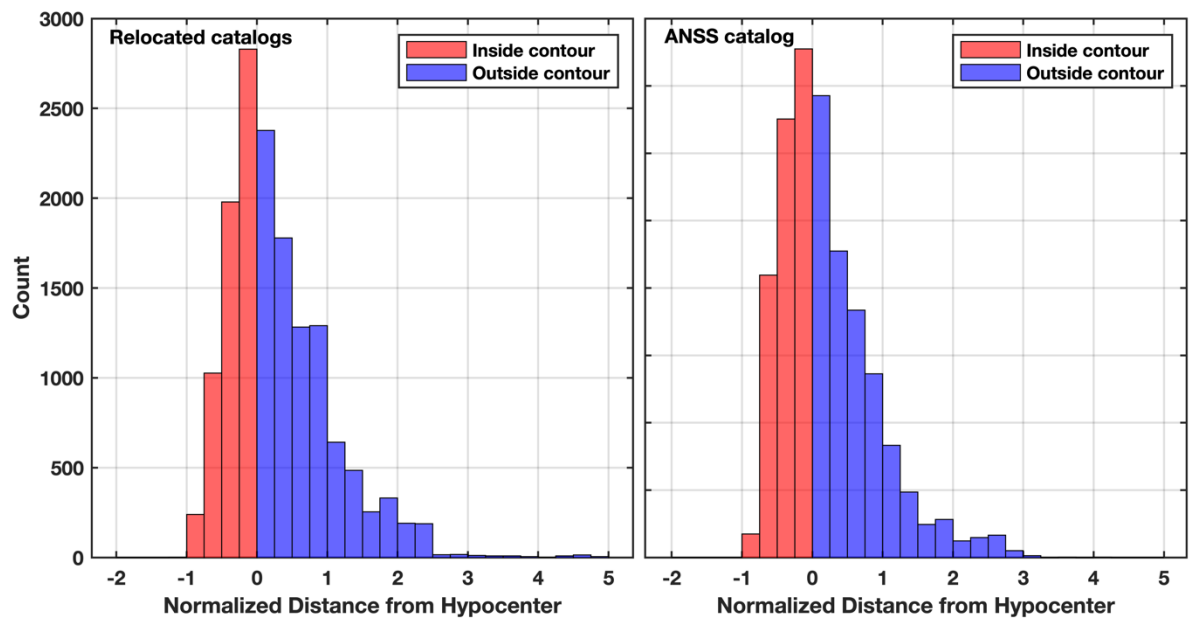


Figure 9. Robust fitting (solid line) and least squares fitting (dashed line) of ratios of Coulomb stress area to aftershock zone area with magnitude.



**Figure 10.** Illustration of how the distances from slip contour are calculated using the Parkfield, Chen Ji et al slip model.



**Figure 11.** Histogram of aftershock distances from slip contours for all earthquakes using the relocated and ANSS catalogs.